

## Structural and Spectroscopic Studies of Valence-Delocalized Diiron(II,III) Complexes Supported by Carboxylate-Only Bridging Ligands

Dongwhan Lee,<sup>†</sup> Jennifer L. DuBois,<sup>‡</sup> Brad Pierce,<sup>§</sup> Britt Hedman,<sup>\*,†,||</sup> Keith O. Hodgson,<sup>\*,†,||</sup> Michael P. Hendrich,<sup>\*,§</sup> and Stephen J. Lippard<sup>\*,†</sup>

Department of Chemistry, Massachusetts Institute of Technology,  
Cambridge, Massachusetts 02139, Department of Chemistry, Stanford University,  
Stanford, California 94305, Stanford Synchrotron Radiation Laboratory, SLAC,  
Stanford University, Stanford, California 94309, and Department of Chemistry,  
Carnegie Mellon University, Pittsburgh, Pennsylvania 15213

Received October 12, 2001

The synthesis, molecular structures, and spectroscopic properties of a series of valence-delocalized diiron(II,III) complexes are described. One-electron oxidation of diiron(II) tetracarboxylate complexes afforded the compounds  $[\text{Fe}_2(\mu\text{-O}_2\text{CAR}^{\text{To}})_4\text{L}_2]\text{X}$ , where  $\text{L} = 4\text{-}^1\text{BuC}_5\text{H}_4\text{N}$  (**1b**),  $\text{C}_5\text{H}_5\text{N}$  (**2b**), and THF (**3b**);  $\text{X} = \text{PF}_6^-$  (**1b** and **3b**) and  $\text{OTf}^-$  (**2b**). In **1b–3b**, four  $\mu\text{-1,3}$  carboxylate ligands span relatively short  $\text{Fe}\cdots\text{Fe}$  distances of 2.6633(11)–2.713(3) Å. Intense ( $\epsilon = 2700\text{--}3200\text{ M}^{-1}\text{ cm}^{-1}$ ) intervalence charge transfer bands were observed at 620–670 nm. EPR spectroscopy confirmed the  $S = 1/2$  ground spin state of **1b–3b**, the valence-delocalized nature of which was probed by X-ray absorption spectroscopy. The electron delocalization between paramagnetic metal centers is described by double exchange, which, for the first time, is observed in diiron clusters having no single-atom bridging ligand(s).

## Introduction

Metalloproteins having valence-delocalized  $\text{Cu}_2(\text{I,II})$  or  $\text{Fe}_2(\text{II,III})$  sites are important participants in biological electron transfer (ET) reactions.<sup>1–3</sup> By delocalizing the charge over multiple nuclei, distortions associated with redox processes are significantly reduced, thus lowering Franck–Condon barriers for ET.<sup>4</sup> Electron trafficking through such clusters is tightly regulated by a delicate interplay between geometric and electronic factors, the understanding of which has been greatly assisted by bioinorganic modeling studies.<sup>2,3,5,6</sup>

The  $\text{Cu}_A$  centers in cytochrome *c* oxidase and nitrous oxide reductase use the  $\text{Cu(I)Cu(II)/Cu}_2(\text{I,II})^7$  redox couple for inter- and intraprotein ET.<sup>8–10</sup> The short  $\text{Cu}\cdots\text{Cu}$  distances ( $\sim 2.44$  Å) revealed by X-ray crystallography<sup>11</sup> indicate direct  $\text{Cu–Cu}$  bonding, which is crucial for valence delocalization at low-symmetry protein sites.<sup>12</sup> Comparison with a model complex<sup>13</sup> suggests that overlap between  $3d_{x^2-y^2}$  orbitals is

\* Authors to whom correspondence should be addressed. E-mail: lippard@lippard.mit.edu (S.J.L.).

<sup>†</sup> Department of Chemistry, Massachusetts Institute of Technology.

<sup>‡</sup> Department of Chemistry, Stanford University.

<sup>§</sup> Department of Chemistry, Carnegie Mellon University.

<sup>||</sup> Stanford Synchrotron Radiation Laboratory, SLAC, Stanford University.

- (1) Holm, R. H.; Kennepohl, P.; Solomon, E. I. *Chem. Rev.* **1996**, *96*, 2239–2314.
- (2) Solomon, E. I.; Hanson, M. A. In *Inorganic Electronic Structure and Spectroscopy*; Solomon, E. I., Lever, A. B. P., Eds.; John Wiley & Sons: New York, 1999; Vol. II, pp 1–129.
- (3) Solomon, E. I.; Randall, D. W.; Glaser, T. *Coord. Chem. Rev.* **2000**, *200*–202, 595–632.
- (4) Marcus, R. A.; Sutin, N. *Biochim. Biophys. Acta* **1985**, *811*, 265–322.
- (5) Beinert, H.; Holm, R. H.; Münck, E. *Science* **1997**, *277*, 653–659.

- (6) Glaser, T.; Hedman, B.; Hodgson, K. O.; Solomon, E. I. *Acc. Chem. Res.* **2000**, *33*, 859–868.
- (7)  $\text{Cu}_2(\text{I,II})$  denotes a valence-delocalized  $\text{Cu(I)Cu(II)}$  center, which can be more appropriately described as  $\text{Cu(1.5)Cu(1.5)}$ . In a similar way,  $\text{Fe}_2(\text{II,III})$  represents a valence-delocalized  $\text{Fe(II)Fe(III)}$  core.
- (8) Ramirez, B. E.; Malmström, B. G.; Winkler, J. R.; Gray, H. B. *Proc. Natl. Acad. Sci. U.S.A.* **1995**, *92*, 11949–11951.
- (9) Ferguson-Miller, S.; Babcock, G. T. *Chem. Rev.* **1996**, *96*, 2889–2907.
- (10) Beinert, H. *Eur. J. Biochem.* **1997**, *245*, 521–532.
- (11) (a) Iwata, S.; Ostermeier, C.; Ludwig, B.; Michel, H. *Nature* **1995**, *376*, 660–669. (b) Tsukihara, T.; Aoyama, H.; Yamashita, E.; Tomizaki, T.; Yamaguchi, H.; Shinzawa-Itoh, K.; Nakashima, R.; Yaono, R.; Yoshikawa, S. *Science* **1995**, *269*, 1069–1074. (c) Tsukihara, T.; Aoyama, H.; Yamashita, E.; Tomizaki, T.; Yamaguchi, H.; Shinzawa-Itoh, K.; Nakashima, R.; Yaono, R.; Yoshikawa, S. *Science* **1996**, *272*, 1136–1144. (d) Brown, K.; Tegoni, M.; Prudêncio, M.; Pereira, A. S.; Besson, S.; Moura, J. J.; Moura, I.; Cambillau, C. *Nature Struct. Biol.* **2000**, *7*, 191–195.
- (12) Gamelin, D. R.; Randall, D. W.; Hay, M. T.; Houser, R. P.; Mulder, T. C.; Canters, G. W.; de Vries, S.; Tolman, W. B.; Lu, Y.; Solomon, E. I. *J. Am. Chem. Soc.* **1998**, *120*, 5246–5263.

responsible for strong electronic coupling in Cu<sub>A</sub>, although indirect superexchange via bridging cysteine thiolate ligands also occurs.<sup>12</sup>

Iron–sulfur clusters in electron transferases participate in many biological ET processes.<sup>5,10</sup> The sulfido bridging ligands in [2Fe–2S] clusters mediate strong antiferromagnetic coupling and afford valence-trapped Fe(II)Fe(III) units upon reduction of the metal center.<sup>14,15</sup> Similar vibronic trapping is responsible for the  $S = 1/2$  ground spin state for oxo- or hydroxo-bridged Fe(II)Fe(III) centers.<sup>16–19</sup> Valence-delocalized Fe<sub>2</sub>(II,III)<sup>7</sup> units with a ground spin state of  $S = 9/2$ , however, occur in two mutant forms of a [2Fe–2S] ferredoxin,<sup>20,21</sup> and at [2Fe–2S] subsites within mixed-valence [4Fe–4S] or [3Fe–4S] clusters.<sup>14</sup> This interesting phenomenon, whereby valence localization shifts to delocalization upon formal dimerization of the {Fe<sub>2</sub>S<sub>2</sub>}<sup>+</sup> units, has yet to be understood.<sup>22</sup> The resonance energy associated with valence delocalization affects the cluster redox potential<sup>23,24</sup> as well as the rate of ET.<sup>25</sup>

Studies of discrete valence-delocalized Fe<sub>2</sub>(II,III) complexes can provide insights into the physical origin of parallel spin alignment observed in biological systems. Prior to this work, few synthetic diiron complexes, [Fe<sub>2</sub>(μ-OH)<sub>3</sub>–(Me<sub>3</sub>TACN)<sub>2</sub>]<sup>2+</sup> (A),<sup>26,27</sup> [L<sup>1</sup>Fe<sub>2</sub>(μ-OAc)<sub>2</sub>]<sup>+</sup> (B),<sup>26,28</sup> and [Fe<sub>2</sub>(μ-O<sup>i</sup>Pr)<sub>2</sub>(μ-O<sub>2</sub>CAr<sup>Mes</sup>)(O<sub>2</sub>CAr<sup>Mes</sup>)<sub>2</sub>] (C),<sup>26,29</sup> were structurally characterized, having  $S = 9/2$  ground spin states that

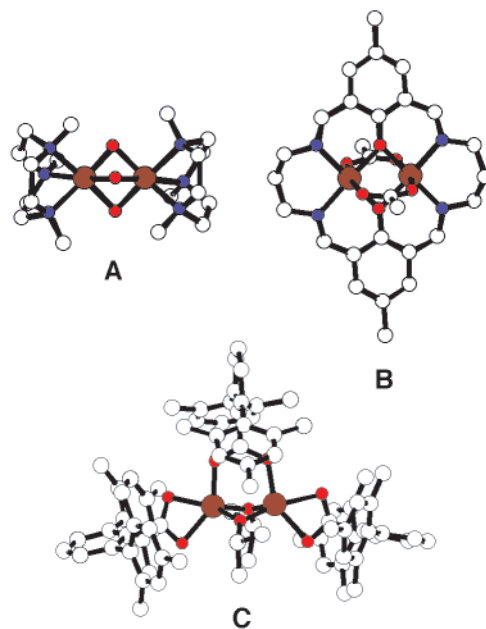


**Figure 1.** Solid-state structures of the cations in [(Me<sub>3</sub>TACN)<sub>2</sub>Fe<sub>2</sub>(μ-OH)<sub>3</sub>](ClO<sub>4</sub>)<sub>2</sub> (A),<sup>27d</sup> [L<sup>1</sup>Fe<sub>2</sub>(μ-OAc)<sub>2</sub>](ClO<sub>4</sub>) (B),<sup>28a</sup> and [Fe<sub>2</sub>(μ-O<sup>i</sup>Pr)<sub>2</sub>(μ-O<sub>2</sub>CAr<sup>Mes</sup>)(O<sub>2</sub>CAr<sup>Mes</sup>)<sub>2</sub>] (C),<sup>29</sup> generated using the crystallographic coordinates, where N is blue, O is bright red, and Fe is dark red.

arise from valence-delocalized Fe<sub>2</sub>(II,III) cores (Figure 1). Various spectroscopic techniques were applied to understand the magnetic and electronic interactions between the metal centers in these compounds. Mössbauer spectroscopy provided the most compelling evidence for equivalent iron sites within the valence-delocalized Fe<sub>2</sub>(II,III) cores.<sup>27b,28a,29</sup> In addition, Fe L-edge X-ray absorption spectroscopy (XAS) was employed to probe the electronic structure of valence-trapped and -delocalized Fe(II)Fe(III) complexes.<sup>27c</sup> Although Fe K-edge and preedge (1s → 3d region) XAS both can provide geometric and electronic structural information,<sup>2,30</sup> this technique has not been used to address issues concerning electron delocalization in iron dimers.

Previously, we communicated the first example of valence-delocalized Fe<sub>2</sub>(II,III) complexes having no single-atom bridging ligand(s).<sup>31</sup> One-electron oxidation of tetracarboxylate diiron(II) precursor compounds afforded a series of (μ-1,3-carboxylato)diiron(II,III) complexes, the  $S = 9/2$  ground spin state of which was indicated by magnetic susceptibility measurements. Characteristic six-line patterns were observed in magnetic Mössbauer spectra recorded at 4.2 K, revealing that the extra electron in the  $S = 9/2$  spin system is delocalized over two metal centers. The iron atoms are thus rendered equivalent on the Mössbauer time scale (~10<sup>–7</sup> s). In this paper, we present a full description of the synthesis and

- (13) Houser, R. P.; Young, V. G., Jr.; Tolman, W. B. *J. Am. Chem. Soc.* **1996**, *118*, 2101–2102.
- (14) Münck, E.; Papaefthymiou, V.; Surerus, K. K.; Girerd, J.-J. In *Metal Clusters in Proteins*; Que, L., Jr., Ed.; American Chemical Society: Washington, DC, 1988; pp 302–325.
- (15) Blondin, B.; Girerd, J.-J. *Chem. Rev.* **1990**, *90*, 1359–1376.
- (16) Bossek, U.; Hummel, H.; Weyhermüller, T.; Bill, E.; Wieghardt, K. *Angew. Chem., Int. Ed. Engl.* **1995**, *34*, 2642–2645.
- (17) Davydov, R. M.; Ménage, S.; Fontecave, M.; Gräslund, A.; Ehrenberg, A. *J. Biol. Inorg. Chem.* **1997**, *2*, 242–255.
- (18) (a) Cohen, J. D.; Payne, S.; Hagen, K. S.; Sanders-Loehr, J. *J. Am. Chem. Soc.* **1997**, *119*, 2960–2961. (b) Payne, S. C.; Hagen, K. S. *J. Am. Chem. Soc.* **2000**, *122*, 6399–6410.
- (19) Mizoguchi, T. J.; Davydov, R. M.; Lippard, S. J. *Inorg. Chem.* **1999**, *38*, 4098–4103.
- (20) Achim, C.; Golinelli, M.-P.; Bominaar, E. L.; Meyer, J.; Münck, E. *J. Am. Chem. Soc.* **1996**, *118*, 8168–8169.
- (21) Achim, C.; Bominaar, E. L.; Meyer, J.; Peterson, J.; Münck, E. *J. Am. Chem. Soc.* **1999**, *121*, 3704–3714.
- (22) Glaser, T.; Rose, K.; Shadle, S. E.; Hedman, B.; Hodgson, K. O.; Solomon, E. I. *J. Am. Chem. Soc.* **2001**, *123*, 442–454.
- (23) Girerd, J.-J. *J. Chem. Phys.* **1983**, *79*, 1766–1775.
- (24) Mouesca, J. M.; Chen, J. L.; Noodleman, L.; Bashford, D.; Case, D. A. *J. Am. Chem. Soc.* **1994**, *116*, 11898–11914.
- (25) Achim, C.; Bominaar, E. L.; Münck, E. *J. Biol. Inorg. Chem.* **1998**, *3*, 126–134.
- (26) Abbreviations used: Me<sub>3</sub>TACN, 1,4,7-trimethyl-1,4,7-triazacyclononane; L<sup>1</sup>, [2 + 2] condensation product of propylenediamine and 2,6-diformyl-4-methylphenoxide; Ar<sup>Mes</sup>CO<sub>2</sub><sup>–</sup>, 2,6-dimesitylbenzoate; Ar<sup>4-FPh</sup>CO<sub>2</sub><sup>–</sup>, 2,6-di(4-fluorophenyl)benzoate; RNR-R2, the R2 subunit of ribonucleotide reductase.
- (27) (a) Drücke, S.; Chaudhuri, P.; Pohl, K.; Wieghardt, K.; Ding, X.-Q.; Bill, E.; Sawaryn, A.; Trautwein, A. X.; Winkler, H.; Gurman, S. J. *J. Chem. Soc., Chem. Commun.* **1989**, 59–62. (b) Ding, X.-Q.; Bominaar, E. L.; Bill, E.; Winkler, H.; Trautwein, A. X.; Drücke, S.; Chaudhuri, P.; Wieghardt, K. *J. Chem. Phys.* **1990**, *92*, 178–186. (c) Peng, G.; van Elp, J.; Jang, H.; Que, L., Jr.; Armstrong, W. H.; Cramer, S. P. *J. Am. Chem. Soc.* **1995**, *117*, 2515–2519. (d) Gamelin, D. R.; Bominaar, E. L.; Kirk, M. L.; Wieghardt, K.; Solomon, E. I. *J. Am. Chem. Soc.* **1996**, *118*, 8085–8097. (e) Gamelin, D. R.; Bominaar, E. L.; Mathonière, C.; Kirk, M. L.; Wieghardt, K.; Girerd, J.-J.; Solomon, E. I. *Inorg. Chem.* **1996**, *35*, 4323–4335. (f) Knapp, M. J.; Krzystek, J.; Brunel, L.-C.; Hendrickson, D. N. *Inorg. Chem.* **1999**, *38*, 3321–3328.

- (28) (a) Dutta, S. K.; Ensling, J.; Werner, R.; Flörke, U.; Haase, W.; Gütlich, P.; Nag, K. *Angew. Chem., Int. Ed. Engl.* **1997**, *36*, 152–155. (b) Saal, C.; Böhm, M. C.; Haase, W. *Inorg. Chim. Acta* **1999**, *291*, 82–90.
- (29) Hagadorn, J. R.; Que, L., Jr.; Tolman, W. B.; Prisecaru, I.; Münck, E. *J. Am. Chem. Soc.* **1999**, *121*, 9760–9761.
- (30) Scott, R. A. In *Physical Methods in Bioinorganic Chemistry: Spectroscopy and Magnetism*; Que, L., Jr., Ed.; University Science Books: Sausalito, CA, 2000; pp 465–503.
- (31) Lee, D.; Krebs, C.; Huynh, B. H.; Hendrich, M. P.; Lippard, S. J. *J. Am. Chem. Soc.* **2000**, *122*, 5000–5001.

spectroscopic properties of the compounds  $[\text{Fe}_2(\mu\text{-O}_2\text{CAr}^{\text{Tot}})_4\text{L}_2]\text{X}$ , where  $\text{Ar}^{\text{Tot}}\text{CO}_2^- = 2,6\text{-di}(p\text{-tolyl})\text{benzoate}$ ;  $\text{L} = 4\text{-}^t\text{BuC}_5\text{H}_4\text{N}$  (**1b**),  $\text{C}_5\text{H}_5\text{N}$  (**2b**), and THF (**3b**);  $\text{X} = \text{PF}_6^-$  (**1b** and **3b**) and  $\text{OTf}^-$  (**2b**). XAS studies disclosed the valence-delocalized nature of **1b–3b**, further substantiating the previous assignment made by Mössbauer spectroscopy. Notably, the “extra” electron in the  $\text{Fe}_2(\text{II,III})$  clusters remains delocalized even in the X-ray photoexcited states, demonstrating that XAS can be a useful probe for investigating this class of compounds.

## Experimental Section

**General Considerations.** All reagents were obtained from commercial suppliers and used as received unless otherwise noted. Dichloromethane was distilled over  $\text{CaH}_2$  under nitrogen. Diethyl ether, pentanes, and THF were saturated with nitrogen and purified by passage through activated  $\text{Al}_2\text{O}_3$  columns under nitrogen.<sup>32</sup> The compounds  $[\text{Fe}_2(\mu\text{-O}_2\text{CAr}^{\text{Tot}})_4(4\text{-}^t\text{BuC}_5\text{H}_4\text{N})_2]$  (**1a**),<sup>33</sup>  $[\text{Fe}_2(\mu\text{-O}_2\text{CAr}^{\text{Tot}})_2(\text{O}_2\text{CAr}^{\text{Tot}})_2(\text{C}_5\text{H}_5\text{N})_2]$  (**2a**),<sup>34</sup>  $[\text{Fe}_2(\mu\text{-O}_2\text{CAr}^{\text{Tot}})_2(\text{O}_2\text{CAr}^{\text{Tot}})_2(\text{THF})_2]$  (**3a**),<sup>34</sup> and  $[\text{Fe}_2(\mu\text{-OH})_2(\mu\text{-O}_2\text{CAr}^{\text{Tot}})_2(\text{O}_2\text{CAr}^{\text{Tot}})_2(4\text{-}^t\text{BuC}_5\text{H}_4\text{N})_2]$  (**1c**)<sup>33</sup> were prepared as described previously. All synthetic procedures and air-sensitive manipulations were carried out under nitrogen in a Vacuum Atmospheres drybox or by standard Schlenk line techniques.

**$[\text{Fe}_2(\mu\text{-O}_2\text{CAr}^{\text{Tot}})_4(4\text{-}^t\text{BuC}_5\text{H}_4\text{N})_2](\text{PF}_6)$  (**1b**).** To a rapidly stirred deep yellow  $\text{CH}_2\text{Cl}_2$  solution (5 mL) of **1a** (128 mg, 81  $\mu\text{mol}$ ) was added dropwise a  $\text{CH}_2\text{Cl}_2$  (3 mL) suspension of  $[\text{Cp}_2\text{Fe}](\text{PF}_6)$  (30 mg, 91  $\mu\text{mol}$ ). The reaction mixture was dark emerald green following the addition. The solution was stirred for 1 h, and volatile fractions were removed under reduced pressure. The solid residue was washed with pentanes (10 mL) and filtered. Recrystallization from  $\text{CH}_2\text{Cl}_2$ /pentanes afforded **1b** (86 mg, 50  $\mu\text{mol}$ , 62%) as dark green microcrystalline material, which was analyzed by X-ray crystallography. FT-IR (KBr,  $\text{cm}^{-1}$ ): 3024, 2962, 2923, 2870, 1618, 1583, 1514, 1497, 1440, 1405, 1386, 1306, 1272, 1232, 1211, 1187, 1153, 1110, 1069, 1030, 844, 810, 792, 762, 728, 704, 586, 557, 530, 488. UV–vis ( $\text{CH}_2\text{Cl}_2$ ,  $\lambda_{\text{max}}$ , nm ( $\epsilon$ ,  $\text{M}^{-1}\text{cm}^{-1}$ ): 670 (3200), 450 (sh, 1600), 380 (sh, 3100). Anal. Calcd for  $\text{C}_{102}\text{H}_{94}\text{N}_2\text{O}_8\text{F}_6\text{-Fe}_2\text{P}$ : C, 70.71; H, 5.47; N, 1.62. Found: C, 71.16; H, 5.85; N, 1.62.

**$[\text{Fe}_2(\mu\text{-O}_2\text{CAr}^{\text{Tot}})_4(\text{C}_5\text{H}_5\text{N})_2](\text{OTf})$  (**2b**).** To a rapidly stirred  $\text{CH}_2\text{Cl}_2$  (5 mL) suspension of **2a** (113 mg, 77  $\mu\text{mol}$ ) was added dropwise  $\text{AgOTf}$  (22 mg, 88  $\mu\text{mol}$ ) suspended in  $\text{CH}_2\text{Cl}_2$  (5 mL). The heterogeneous mixture was stirred for 1 h and filtered through Celite. The dark green filtrate was concentrated to ca. 5 mL. Vapor diffusion of pentanes into the resulting solution afforded dark brown crystals of **2b** (90 mg, 55  $\mu\text{mol}$ , 71%), which were suitable for X-ray crystallography. FT-IR (KBr,  $\text{cm}^{-1}$ ): 3025, 2919, 1610, 1583, 1513, 1485, 1437, 1406, 1384, 1304, 1265, 1222, 1184, 1265, 1222, 1184, 1148, 1110, 1067, 1044, 1031, 1016, 845, 814, 790, 761, 727, 712, 704, 692, 636, 584, 528, 487, 416. UV–vis ( $\text{CH}_2\text{Cl}_2$ ,  $\lambda_{\text{max}}$ , nm ( $\epsilon$ ,  $\text{M}^{-1}\text{cm}^{-1}$ ): 665 (2900), 455 (sh, 1800), 385 (sh, 3400). Anal. Calcd for  $\text{C}_{95}\text{H}_{78}\text{N}_2\text{O}_{11}\text{F}_3\text{Fe}_2\text{S}$ : C, 70.24; H, 4.84; N, 1.72. Found: C, 70.62; H, 4.98; N, 1.64.

**$[\text{Fe}_2(\mu\text{-O}_2\text{CAr}^{\text{Tot}})_4(\text{THF})_2](\text{PF}_6)$  (**3b**).** This compound was prepared from **3a** (154 mg, 105  $\mu\text{mol}$ ) and  $[\text{Cp}_2\text{Fe}](\text{PF}_6)$  (40 mg, 121  $\mu\text{mol}$ ) by a procedure analogous to that used to obtain **1b**. Blue-

purple blocks (117 mg, 73  $\mu\text{mol}$ , 60%) were afforded following vapor diffusion of pentanes into the  $\text{CH}_2\text{Cl}_2$  solution of this material. Single crystals suitable for X-ray crystallography were obtained similarly from pentanes and a chlorobenzene solution of this material. FT-IR (KBr,  $\text{cm}^{-1}$ ): 3025, 2919, 1583, 1566, 1521, 1436, 1382, 1305, 1270, 1236, 1210, 1190, 1154, 1110, 1076, 1019, 957, 917, 860, 761, 727, 705, 585, 556, 528, 492. UV–vis ( $\text{CH}_2\text{Cl}_2$ ,  $\lambda_{\text{max}}$ , nm ( $\epsilon$ ,  $\text{M}^{-1}\text{cm}^{-1}$ ): 620 (2700), 450 (sh, 1600), 385 (sh, 3200). Anal. Calcd for  $\text{C}_{92}\text{H}_{84}\text{O}_{10}\text{F}_6\text{Fe}_2\text{P}$ : C, 68.79; H, 5.27. Found: C, 68.23; H, 5.39.

**X-ray Crystallographic Studies.** Intensity data were collected on a Bruker (formerly Siemens) CCD diffractometer with graphite-monochromated  $\text{Mo K}\alpha$  radiation ( $\lambda = 0.71073\text{ \AA}$ ), controlled by a Pentium-based PC running the SMART software package.<sup>35</sup> Single crystals were mounted at room temperature on the tips of quartz fibers, coated with Paratone-N oil, and cooled to 188 K under a cold stream of nitrogen maintained by a Bruker LT-2A nitrogen cryostat. Data collection and reduction protocols are described elsewhere.<sup>36</sup> Empirical absorption corrections were applied with SADABS,<sup>37</sup> part of the SHELXTL program package. The possibility of higher symmetry was checked by the program PLATON.<sup>38</sup> All non-hydrogen atoms were refined anisotropically unless otherwise noted. Hydrogen atoms were assigned idealized positions and given thermal parameters equivalent to either 1.5 (methyl hydrogen atoms) or 1.2 (all other hydrogen atoms) times the thermal parameter of the carbon atom to which they are attached. The hydrogen atoms associated with the disordered solvent molecules were not included in the refinement. The structure of **2b** contains a lattice  $\text{CH}_2\text{Cl}_2$  molecule, disordered over three positions, which was refined isotropically. In the structure of **3b**, each coordinated THF molecule contains two carbon atoms disordered over two positions. In each case the atoms were distributed over two positions and refined isotropically. The  $\text{PF}_6^-$  anion in the structure of **3b** is disordered over two positions and was refined isotropically. The structure of **1b** was not fully refined owing to severe disorder in the  $\text{PF}_6^-$  counterion and the solvent molecules.

**Physical Measurements.** FT-IR spectra were recorded on a Bio Rad FTS-135 instrument with Win-IR software. UV–vis spectra were recorded on a Hewlett-Packard 8453 diode array spectrophotometer. UV–vis–NIR spectra were obtained using a Cary 17 spectrophotometer modified by On-Line Instrument Systems (OLIS) to introduce computer control.

**Electrochemistry.** Cyclic voltammetric measurements were carried out in a Vacuum Atmospheres drybox under nitrogen with an EG&G model 263 potentiostat. A three-electrode configuration consisting of a 1.75-mm<sup>2</sup> platinum working electrode, a  $\text{Ag}/\text{AgNO}_3$  (0.1 M in MeCN with 0.5 M  $(\text{Bu}_4\text{N})\text{PF}_6$ ) reference electrode, and a platinum mesh auxiliary electrode was used. The supporting electrolyte was 0.5 M  $(\text{Bu}_4\text{N})\text{PF}_6$  in  $\text{CH}_2\text{Cl}_2$ . All cyclic voltammograms were externally referenced to the  $\text{Cp}_2\text{Fe}/\text{Cp}_2\text{Fe}^+$  couple.

**EPR Spectroscopy.** X-band (9 GHz) EPR spectra were recorded on a Bruker 300 spectrometer equipped with an Oxford ESR 910 cryostat for low-temperature measurement. Q-band (35 GHz) EPR spectra were recorded on a Bruker 200 spectrometer equipped with a locally built low-temperature microwave probe and a cryogenic system.<sup>39</sup> For both instruments, the microwave frequency was

(35) SMART v5.05; Bruker AXS Inc.: Madison, WI, 1998.

(36) Feig, A. L.; Bautista, M. T.; Lippard, S. J. *Inorg. Chem.* **1996**, *35*, 6892–6898.

(37) Sheldrick, G. M. *SADABS v2.03: Area-Detector Absorption Correction*; University of Göttingen: Göttingen, Germany, 1999.

(38) Spek, A. L. *PLATON, A Multipurpose Crystallographic Tool*; Utrecht University: Utrecht, The Netherlands, 1998.

(39) Petasis, D.; Hendrich, M. P. *J. Magn. Reson.* **1999**, *136*, 200–206.

(32) Pangborn, A. B.; Giardello, M. A.; Grubbs, R. H.; Rosen, R. K.; Timmers, F. J. *Organometallics* **1996**, *15*, 1518–1520.

(33) Lee, D.; Du Bois, J.; Petasis, D.; Hendrich, M. P.; Krebs, C.; Huynh, B. H.; Lippard, S. J. *J. Am. Chem. Soc.* **1999**, *121*, 9893–9894.

(34) Lee, D.; Lippard, S. J. *J. Am. Chem. Soc.* **1998**, *120*, 12153–12154.



calibrated by a frequency counter and the magnetic field with a NMR gaussmeter. The temperature of both instruments was calibrated using devices from Lake Shore Cryotronics. For X- and Q-band EPR, the magnetic field modulation was 100 kHz. All experimental data were collected under non-saturation conditions. For all measurements, ~2 mM frozen solutions were prepared in a 1:2 mixture of dichloromethane and 2-chlorobutane, in which the samples formed a nice glass.

**EPR Simulations.** Analysis of the EPR spectra utilized the general spin Hamiltonian of the electronic system (eq 1). Simula-

$$H_s = D \left[ S_z^2 - \frac{S(S+1)}{3} \right] + E(S_x^2 - S_y^2) + \beta \mathbf{B} \cdot \mathbf{g} \cdot \mathbf{S} \quad (1)$$

tions of the EPR spectra were obtained from diagonalization of eq 1 with locally written software. The powder pattern was generated for a uniform spherical distribution of the magnetic field vector **B**. The transition intensities were calculated from the square of the transition moment. The spectral line width was dominated by *D*-strain, and simulations used distributions of the *D* and *E/D* values, specified as  $\sigma_D$  and  $\sigma_{E/D}$ , to give the correct line width. Least-squares and deconvolution analyses of the spectra were combined to allow relevant parameters to vary while maintaining a sum of multiple species that best fit the experimental data. The simulations were generated with careful consideration of all intensity factors, both theoretical and instrumental. This approach allowed direct comparison of simulated spectra to the absolute intensity scale of the experimental spectra having a known sample concentration. The only unknown factor relating the spin concentration to signal intensity is an instrumental one that depends on the microwave detection system. This factor was determined by the spin standard CuEDTA, however, for which the copper concentration was accurately determined by plasma emission spectroscopy.

**X-ray Absorption Spectroscopy (XAS).** X-ray absorption spectra were measured on unfocused wiggler beamline 7-3 at the Stanford Synchrotron Radiation Laboratory (SSRL), with the ring operating at 3 GeV and 50–100 mA. Solid samples of **1a**, **1c**, and **1b–3b** were prepared by grinding ~30 mg of polycrystalline powder with BN and pressing the mixture into a 1 mm thick aluminum sample holder. Samples were maintained at 10 K inside an Oxford Instrument CF-1208 liquid helium continuous flow cryostat. A Si(220) double-crystal monochromator was used, detuned 50% at 7987 eV in order to minimize contamination of the radiation by higher harmonics. Vertical 1-mm premonochromator slits were used to define the beam size, minimizing beam divergence and allowing for an energy resolution of ~1.4 eV at the Fe K-edge. Spectra were measured in transmission mode using dinitrogen-filled ionization chambers. The spectrum of Fe foil was collected concomitantly, allowing for internal energy calibration of the data. The first inflection point energy for the Fe foil spectrum was set to 7111.2 eV. The reproducibility in the determination of edge position was <0.2 eV. K-edge data were measured over the energy range 7105–7150 eV. Multiple (4–5) scans over the complete energy range were averaged for each sample. For each spectrum, a smooth second-order polynomial was fit to the preedge region, then extrapolated across the entire energy range, and subtracted from the data.

## Results

**Electrochemistry of [Fe<sub>2</sub>(μ-O<sub>2</sub>CAr<sup>Tol</sup>)<sub>4</sub>(4-<sup>t</sup>BuC<sub>5</sub>H<sub>4</sub>N)<sub>2</sub>] (1a) and [Fe<sub>2</sub>(μ-O<sub>2</sub>CAr<sup>Tol</sup>)<sub>2</sub>(O<sub>2</sub>CAr<sup>Tol</sup>)<sub>2</sub>(THF)<sub>2</sub>] (3a).** Electrochemical properties of **1a** and **3a** were investigated by cyclic voltammetry, in order to select appropriate one-

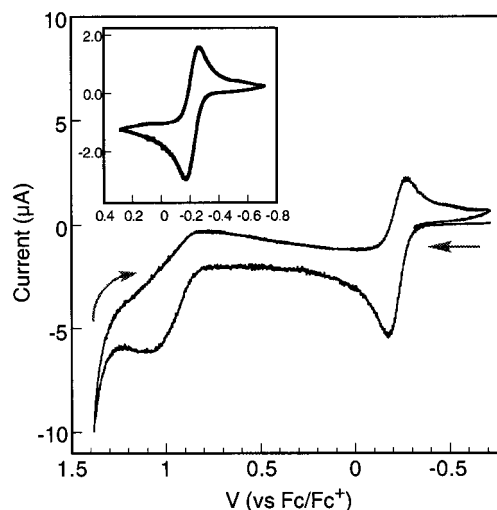
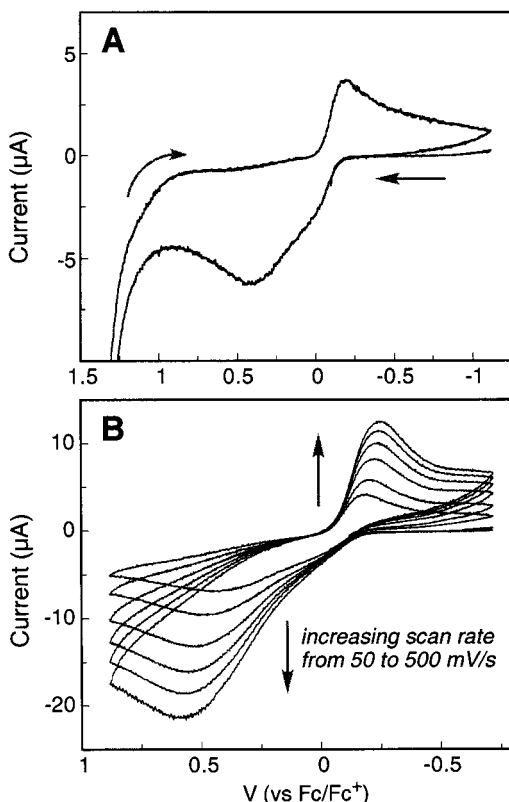


**Figure 2.** Cyclic voltammograms of [Fe<sub>2</sub>(μ-O<sub>2</sub>CAr<sup>Tol</sup>)<sub>4</sub>(4-<sup>t</sup>BuC<sub>5</sub>H<sub>4</sub>N)<sub>2</sub>] (**1a**) in CH<sub>2</sub>Cl<sub>2</sub> with 0.5 M (Bu<sub>4</sub>N)(PF<sub>6</sub>) as supporting electrolyte and a scan rate of 50 mV/s. The inset shows the reversible wave observed when the experiment was conducted at potentials below +300 mV vs Fc/Fc<sup>+</sup> (scan rate = 25 mV/s).

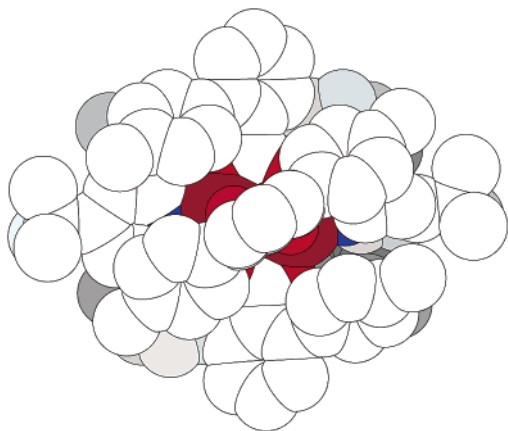
electron chemical oxidants to access the Fe(II)Fe(III) oxidation states. Measurement was not made with **2a**, due to its limited solubility in CH<sub>2</sub>Cl<sub>2</sub>. Cyclic voltammograms of a CH<sub>2</sub>Cl<sub>2</sub> solution of **1a** revealed a reversible oxidation at  $E_{1/2} = -216$  mV vs Cp<sub>2</sub>Fe<sup>+</sup>/Cp<sub>2</sub>Fe ( $\Delta E_p = 89$  mV) (Figure 2). A broad second oxidation wave occurs at ca. +1080 mV, which does not display a corresponding reduction wave in the return sweep. Under identical conditions, the compound [Fe<sub>2</sub>(μ-O<sub>2</sub>CAr<sup>4-FPh</sup>)<sub>4</sub>(4-<sup>t</sup>BuC<sub>5</sub>H<sub>4</sub>N)<sub>2</sub>]<sup>26,40</sup> exhibited a similarly reversible oxidation step at  $E_{1/2} = -16$  mV vs Cp<sub>2</sub>Fe<sup>+</sup>/Cp<sub>2</sub>Fe ( $\Delta E_p = 97$  mV) (Figure S1, Supporting Information). A positive shift ( $\Delta E = +200$  mV) in the oxidation potential is consistent with the coordination of less electron-donating fluoro-substituted ligands Ar<sup>4-FPh</sup>CO<sub>2</sub><sup>-</sup>. A similar shift would place the second oxidation peak of [Fe<sub>2</sub>(μ-O<sub>2</sub>CAr<sup>4-FPh</sup>)<sub>4</sub>(4-<sup>t</sup>BuC<sub>5</sub>H<sub>4</sub>N)<sub>2</sub>] at +1280 mV, lying at the positive limit of the accessible potential window. No second oxidation step was observed. Compound **3a** displayed a broad oxidation wave, beginning at -150 mV and maximizing at +400 mV. A significantly narrower reduction wave occurred at -195 mV in the return sweep (Figure 3A). Similarly irreversible redox behavior was observed even with increased scan rates (50–500 mV/s) at a narrower potential sweep range from -720 to +880 mV (Figure 3B).

**Synthesis and Structural Characterization of [Fe<sub>2</sub>(μ-O<sub>2</sub>CAr<sup>Tol</sup>)<sub>4</sub>(4-<sup>t</sup>BuC<sub>5</sub>H<sub>4</sub>N)<sub>2</sub>](PF<sub>6</sub>) (1b), [Fe<sub>2</sub>(μ-O<sub>2</sub>CAr<sup>Tol</sup>)<sub>4</sub>(C<sub>5</sub>H<sub>5</sub>N)<sub>2</sub>](OTf) (2b), and [Fe<sub>2</sub>(μ-O<sub>2</sub>CAr<sup>Tol</sup>)<sub>4</sub>(THF)<sub>2</sub>](PF<sub>6</sub>) (3b).** Reactions of **1a–3a** with 1 equiv of [Cp<sub>2</sub>Fe]PF<sub>6</sub> or AgOTf in CH<sub>2</sub>Cl<sub>2</sub> resulted in an instantaneous color change from yellow to deep forest green. Dark brown-green blocks of **1b–3b** were obtained in good yield (60–71%), following recrystallization from CH<sub>2</sub>Cl<sub>2</sub>/pentanes. These compounds are stable both in the solid state and in solution when protected from exposure to dioxygen or to coordinating solvents such as THF, MeCN, or MeOH. Attempts to access a similar

(40) Lee, D.; Lippard, S. J. *Inorg. Chem.* **2002**, *41*, 827–837.



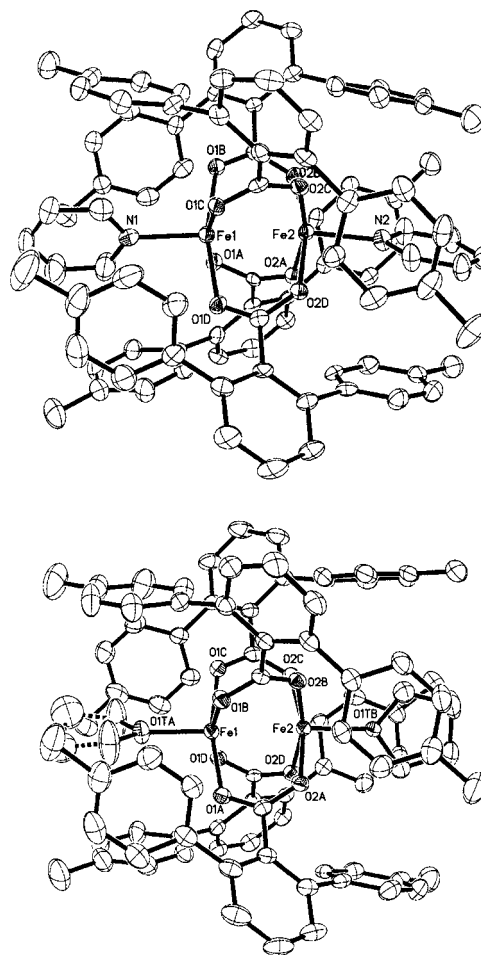
**Figure 3.** Cyclic voltammograms of  $[\text{Fe}_2(\mu\text{-O}_2\text{CAr}^{\text{Tol}})_2(\text{O}_2\text{CAr}^{\text{Tol}})_2(\text{THF})_2]$  (**3a**) in  $\text{CH}_2\text{Cl}_2$  with 0.5 M  $(\text{Bu}_4\text{N})(\text{PF}_6)$  as supporting electrolyte and a scan rate of 50 mV/s (A); with increasing scan rates from 50 to 500 mV/s (B).



**Figure 4.** Space-filling representation of the solid-state structure of the  $[\text{Fe}_2(\mu\text{-O}_2\text{CAr}^{\text{Tol}})_4(4\text{-BuC}_5\text{H}_4\text{N})_2]^+$  cation generated using the crystallographic coordinates, where N is blue, O is bright red, and Fe is dark red.

unit by oxidizing  $[\text{Fe}_2(\mu\text{-O}_2\text{CCMe}_3)_4(\text{C}_5\text{H}_5\text{N})_2]$ <sup>41</sup> with 1 equiv of  $[\text{Cp}_2\text{Fe}]\text{PF}_6$  did not lead to any isolable product. The initial dark green reaction mixture gradually decomposed to an orange brown material. Steric shielding provided by the *m*-terphenyl units (Figure 4) apparently plays a crucial role in stabilizing the mixed valence diiron cores in **1b–3b**.

The solid-state structures of **1b–3b** were determined by X-ray crystallography. The molecular structures are shown

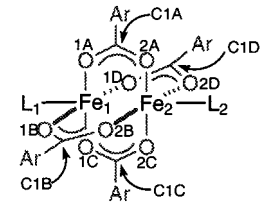


**Figure 5.** ORTEP diagrams of the cation in  $[\text{Fe}_2(\mu\text{-O}_2\text{CAr}^{\text{Tol}})_4(\text{C}_5\text{H}_5\text{N})_2](\text{OTf})$  (**2b**) (top) and  $[\text{Fe}_2(\mu\text{-O}_2\text{CAr}^{\text{Tol}})_4(\text{THF})_2](\text{PF}_6)$  (**3b**) (bottom) with thermal ellipsoids at 50% probability.

in Figures 4 and 5; selected bond lengths and angles are listed in Table 1. Although severe disorder in the  $\text{PF}_6^-$  counterion and solvent molecules hampered detailed structural refinement of the model for **1b**, its  $\text{Fe}\cdots\text{Fe}$  distance of 2.713(3) Å, as well as the quadruply bridged core structure, is comparable to the corresponding properties of **2b** and **3b**. In **1b–3b**, the  $\text{Fe}\cdots\text{Fe}$  distances are 2.6633(11)–2.713(3) Å and four  $\mu$ -1,3 carboxylate ligands bridge the Fe–Fe vector. This architectural feature is shared by a few structurally characterized paddle-wheel diiron(II) complexes.<sup>33,40,41</sup> The two iron atoms are crystallographically inequivalent but display similar square-pyramidal coordination comprising four carboxylate oxygen atoms at the base and one N- or O-donor atom at the axial position. In order to minimize interligand steric repulsions, the benzoate rings in the  $\text{Ar}^{\text{Tol}}\text{CO}_2^-$  ligands are twisted from the  $\text{CO}_2^-$  planes by 39.3–45.7°. This conformation provides tetragonal pockets on either side of the Fe–Fe vector. The motion of the axial ligand confined within this pocket is significantly restricted. The dihedral angles between the two pyridine planes are 72.3° in **1b** and 62.1° in **2b**. Comparable Fe–O<sub>carboxylate</sub> distances were observed for each iron within the dimer (Table 1).

**Electronic Absorption Spectroscopy.** Compounds **1b–3b** display intense visible absorption bands at  $\lambda_{\text{max}} =$

(41) Randall, C. R.; Shu, L.; Chiou, Y.-M.; Hagen, K. S.; Ito, M.; Kitajima, N.; Lachicotte, R. J.; Zang, Y.; Que, L., Jr. *Inorg. Chem.* **1995**, *34*, 1036–1039.

**Table 1.** Selected Bond Lengths (Å) and Angles (deg) for **2b** and **3b**<sup>a</sup>


	<b>2b</b>	<b>3b</b>
Fe1...Fe2	2.6982(13)	2.6633(11)
Fe1—O1A	2.011(3)	2.009(3)
Fe1—O1B	2.008(3)	2.016(3)
Fe1—O1C	2.013(4)	2.007(3)
Fe1—O1D	2.012(4)	2.024(3)
Fe1—L1	2.104(4)	2.011(3)
Fe2—O2A	2.015(3)	2.024(3)
Fe2—O2B	1.989(3)	1.994(3)
Fe2—O2C	2.000(3)	2.016(3)
Fe2—O2D	2.005(3)	2.003(3)
Fe2—L2	2.085(4)	2.017(3)
Fe1—O1A—C1A	121.4(3)	122.1(3)
Fe1—O1B—C1B	125.4(3)	120.6(3)
Fe1—O1C—C1C	123.9(3)	126.1(3)
Fe1—O1D—C1D	122.2(3)	123.1(2)
Fe2—O2A—C1A	126.1(3)	125.0(3)
Fe2—O2B—C1B	122.3(3)	124.9(3)
Fe2—O2C—C1C	123.2(3)	120.8(3)
Fe2—O2D—C1D	123.5(3)	122.8(3)

<sup>a</sup> Numbers in parentheses are estimated standard deviations of the last significant figures.

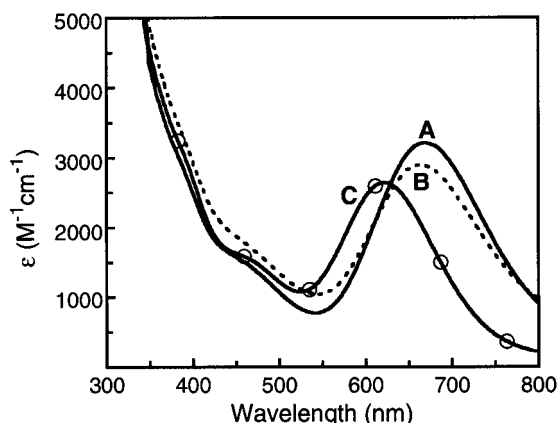


**Figure 6.** Electronic absorption spectra of **1b–3b** in  $\text{CH}_2\text{Cl}_2$  showing the IVCT transitions: (A)  $[\text{Fe}_2(\mu\text{-O}_2\text{CAr}^{\text{Tot}})_4(4\text{-}^i\text{BuC}_5\text{H}_4\text{N})_2](\text{PF}_6)$  (**1b**) (—); (B)  $[\text{Fe}_2(\mu\text{-O}_2\text{CAr}^{\text{Tot}})_4(\text{C}_5\text{H}_5\text{N})_2](\text{OTf})$  (**2b**) (···); (C)  $[\text{Fe}_2(\mu\text{-O}_2\text{CAr}^{\text{Tot}})_4(\text{THF})_2](\text{PF}_6)$  (**3b**) (— with circle).

620–670 nm ( $\epsilon = 2700\text{--}3200 \text{ M}^{-1} \text{ cm}^{-1}$ ) and two shoulders at  $\sim 380 \text{ nm}$  ( $\epsilon = 3100\text{--}3400 \text{ M}^{-1} \text{ cm}^{-1}$ ) and  $\sim 450 \text{ nm}$  ( $\epsilon = 1600\text{--}1800 \text{ M}^{-1} \text{ cm}^{-1}$ ) in  $\text{CH}_2\text{Cl}_2$  (Figure 6; Table 2). No other visible–NIR transitions occur up to 1650 nm (Figure S2, Supporting Information). Since both the pyridine and THF complexes behave similarly, the 620–670 nm bands are assigned as intervalence charge transfer (IVCT), rather than LMCT, transitions. The experimentally determined width at half-height ( $\Delta\nu_{1/2}$ ) ranges between 3590 and 3970  $\text{cm}^{-1}$  for **1b–3b**, values significantly lower than those predicted by Hush's relationship<sup>42,43</sup> for class II mixed

valence centers ( $\Delta\nu_{1/2} = [2310 \nu_{\text{max}}]^{1/2} = 5880\text{--}6120 \text{ cm}^{-1}$ ). This result strongly indicates that **1b–3b** are valence-delocalized diiron(II,III) complexes. Similar IVCT bands are observed at 758–1060 nm ( $\epsilon = 1250\text{--}2400 \text{ M}^{-1} \text{ cm}^{-1}$ ) for **A–C** (Figure 1; Table 2).<sup>27–29</sup>

**EPR Spectroscopy.** Shown in Figure 7 are frozen solution EPR spectra of **1b–3b** measured at X-band and Q-band. Compounds **3b** and **1b** exhibit similar signals at X-band (A and C) with resonances at  $g = 9.5$  and 2.0. These resonances are near the expected values of  $g = 10$  and 2 for the  $m_s = 1/2$  doublet, based on the standard diagram of  $g_{\text{obs}}$  vs  $E/D$  for  $S = 9/2$  complexes with  $E/D \sim 0$ .<sup>44</sup> At Q-band (D and F), three resonances are observed at  $g = 8.9$ , 4.5, and 3.0, which are not the expected  $g$  values for  $E/D \sim 0$ . For  $D \leq h\nu$ , significant mixing of the doublets occurs, which invalidates the standard  $g_{\text{obs}}$  vs  $E/D$  diagram. We thus used simulations to determine the origin of the signals. Each simulation was generated with consideration of all intensity factors, both theoretical and experimental. The spin quantitations obtained by the spectra of Figure 7 were all within 15% of that expected from the diiron complex concentration. Table 3 summarizes the zero-field splitting (zfs) parameters for **1b–3b** as determined from the simulations shown in Figure 7.

The X- and Q-band EPR spectra of **1b** (Figure 7C,F) can be simulated using a unique set of parameters. From the simulations (dashed lines) overlaid on the data, we find  $D = 1.13 \text{ cm}^{-1}$  and  $E/D = 0.007$ . The line widths are dominated by  $D$  strain, which is modeled with distributions in the parameters  $D$  and  $E/D$  of Gaussian width  $\sigma_D$  and  $\sigma_{ED}$ . The spectral simulations determine both parameters independently, with values of  $\sigma_D = 0.02 \text{ cm}^{-1}$  and  $\sigma_{ED} = 0.004$ . The resonances at  $g = 8.9$  and 3.0 are assigned to transitions within the  $m_s = \pm 1/2$  and  $\pm 3/2$  doublets, respectively. The resonance at  $g = 4.5$  arises from an interdoublet transition between the  $m_s = +1/2$  and  $-3/2$  levels. For the Q-band simulations, a sharp feature at  $g = 9.5$  in the simulations does not match the line width in the experimental data. We suspect that this feature is broadened in the experimental data by intermolecular magnetic dipole interactions owing to the formation of small molecular aggregates. This interpretation is supported by the fact that the signal line width strongly depends on the solvent used. Attempts to dissociate these aggregates by using lower sample concentration were not successful. The increased line width of **3b** relative to **1b** is due to a slightly increased rhombicity ( $E/D = 0.011$ ). Unlike **1b**, the Q-band EPR spectrum of **3b** (Figure 7D) lacks the interdoublet transition. This result can be attributed to an increase in  $D$  strain for **3b**. Alternatively, given the differences in the axial donor ligands of **1b** and **3b**, the interdoublet transition expected for **3b** at  $g = 4.5$  could be shifted downfield by decreasing the value of  $D$ . Due to the mixing with the  $m_s = \pm 1/2$  doublet, however, an increase in  $D$  would also shift the signal from the  $m_s = \pm 3/2$  doublet at  $g = 3.0$  downfield. We therefore conclude that the interdoublet transition of **3b** is broadened away by  $D$  strain ( $\sigma_D = 0.08 \text{ cm}^{-1}$ ), not by shifts in the  $D$  value.

(42) Hush, N. S. *Prog. Inorg. Chem.* **1967**, 8, 391–444.

(43) Creutz, C. *Prog. Inorg. Chem.* **1983**, 30, 1–73.

(44) Krebs, C.; Davydov, R.; Baldwin, J.; Hoffman, B. M.; Bollinger, J. M., Jr.; Huynh, B. H. *J. Am. Chem. Soc.* **2000**, 122, 5327–5336.

**Table 2.** Summary of Pertinent Structural and Spectroscopic Data for **1b–3b** and Related Mixed-Valence  $S = 9/2$  Fe<sub>2</sub>(II,III) Systems

	Fe···Fe (Å)	$\lambda_{\text{max}}$ , nm ( $\epsilon$ , M <sup>-1</sup> cm <sup>-1</sup> )	$\Delta\nu_{1/2}$ (cm <sup>-1</sup> )		$\mu_{\text{eff}}/\mu_{\text{B}}$	$\delta$ (mm/s)	$\Delta E_{\text{Q}}$ (mm/s)	ref
			calcd <sup>a</sup>	measd				
<b>1b</b>	2.713(3)	670 (3200) 450 (1600) <sup>b</sup> 380 (3100) <sup>b</sup>	5880	3590	11.0 <sup>c</sup>	0.65	−0.63	31, this work
<b>2b</b>	2.6982(13)	665 (2900) 455 (1800) <sup>b</sup> 385 (3400) <sup>b</sup>	5900	3970	10.2 <sup>c</sup>			31, this work
<b>3b</b>	2.6633(11)	620 (2700) 450 (1600) <sup>b</sup> 385 (3200) <sup>b</sup>	6120	3670	10.5 <sup>c</sup>			31, this work
<b>A</b>	2.509(6)	758 (2400)	5500	3800	10.5 <sup>d</sup>	0.74	−2.14	27a–d
<b>B</b>	2.7414(8)	1060 (1250)	4670	3980	10.0 <sup>e</sup>	0.84	2.09	28a
<b>C</b>	2.6241(9)	780 (2000)				0.76	2.0	29

<sup>a</sup>  $\Delta\nu_{1/2} = [2310 \nu_{\text{max}}]^{1/2}$  (refs 42, 43). <sup>b</sup> Shoulders determined from derivative spectra. <sup>c</sup> 300 K. <sup>d</sup> 30–300 K. <sup>e</sup> 70–300 K.

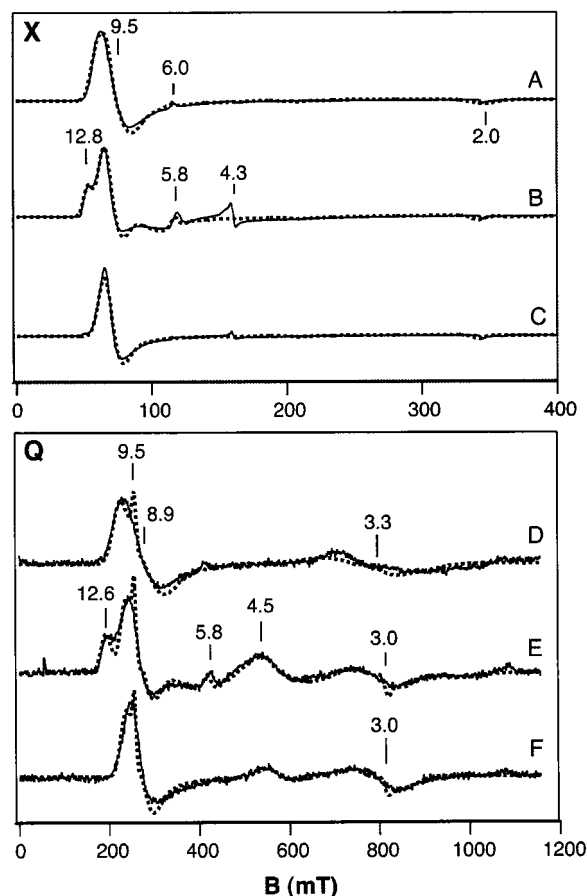


**Figure 7.** X-band (A–C) and Q-band (D–F) EPR spectra (solid lines) of **3b**, **2b**, and **1b**, respectively. The X-band signal observed at  $g = 4.3$  (B) originates from an Fe(III) contaminant (<3% total iron in the sample). Simulations (dashed lines) were calculated for each derivative using zfs parameters listed in Table 3. A minimum line width of 0.3 mT was factored into all simulations. **1b** (C and F); **2b** (B and E); **3b** (A and D). EPR conditions: frequency, 9.62 GHz (X) and 34.2 GHz (Q); power, 0.2 mW and 0.02 mW; modulation amplitude, 1 mT and 0.5 mT; temperature, 11 K (A–C) and 15 K (D–F).

Both X- and Q-band EPR spectra of **2b** (Figure 7B,E) appear markedly different from those of **1b** and **3b**. The new features observed for **2b** near  $g = 12.8$  and 5.8 require additional species having a different rhombicity, the contribution of which to the overall spectral pattern is analyzed in Figure 8. The two spectroscopically distinctive species in the sample of **2b** are described by a set of two unique spectral

**Table 3.** Zero-Field Splitting Parameters of [Fe<sub>2</sub>( $\mu$ -O<sub>2</sub>CAr<sup>Tol</sup>)<sub>4</sub>-(4'-BuC<sub>5</sub>H<sub>4</sub>N)<sub>2</sub>](PF<sub>6</sub>) (**1b**), [Fe<sub>2</sub>( $\mu$ -O<sub>2</sub>CAr<sup>Tol</sup>)<sub>4</sub>(C<sub>5</sub>H<sub>5</sub>N)<sub>2</sub>](OTf) (**2b**), and [Fe<sub>2</sub>( $\mu$ -O<sub>2</sub>CAr<sup>Tol</sup>)<sub>4</sub>(THF)<sub>2</sub>](PF<sub>6</sub>) (**3b**)<sup>a</sup>

	$D$ (cm <sup>-1</sup> )	$\sigma_D$ (cm <sup>-1</sup> )	$E/D$ (cm <sup>-1</sup> )	$\sigma_{E/D}$ (cm <sup>-1</sup> )
<b>1b</b>	1.13	0.020	0.007	0.004
<b>2b</b>				
species 1	1.13	0.020	0.007	0.004
species 2	1.13	0.024	0.026	0.007
<b>3b</b>	1.13	0.081	0.011	0.006

<sup>a</sup> An intrinsic isotropic  $g$  value of 2.026 of eq 1 gave the best fits to the data.

parameters and exist in approximately the same relative amounts. The EPR parameters of  $D = 1.13$  cm<sup>-1</sup> and  $E/D = 0.007$  obtained for species 1 (Figure 8B,E) are comparable to those of **1b** and **3b** (Table 3), whereas species 2 (Figure 8C,F) can be simulated with zfs parameters of  $D = 1.13$  cm<sup>-1</sup> and  $E/D = 0.03$ . The ratio of the signal intensities of species 1 and 2 is not altered up to ~200 K, indicating that both have similarly large energy gaps between the ground ( $S = 9/2$ ) and the first excited ( $S = 7/2$ ) states originating from double exchange. The presence of multiple species of **2b** having distinct  $E/D$  values may be explained by invoking aggregation of the compound in the frozen solution samples. Such an aggregation may distort the local  $D_{4h}$  symmetry of the metal center by perturbing the plane defined by the four carboxylate oxygen donor atoms. Deviation from the axial ( $E/D = 0$ ) magnetic environment would result in the increased rhombicity of species 2 relative to species 1. Detailed information of the structural variations leading to the spectroscopically inequivalent species of **2b**, however, is currently unavailable.

**X-ray Absorption Spectroscopy.** As shown in Figures 9 and 10, the Fe K-edge and preedge (1s  $\rightarrow$  3d transitions) spectra of **1b–3b** are nearly identical and intermediate in energy between K-edges for structurally related diiron(II) complex **1a** and diiron(III) complex **1c**. Adding K-edge spectra for **1a** and **1c** at a weighted ratio of 50:50 yielded a spectrum comparable in rising edge energy to those of **1b–3b** (Figure 10), consistent with the formal description of the oxidation states of the mixed-valence species as Fe(II)-Fe(III). K-edges or preedges for the mixed-valence complexes, however, are not a simple 50:50 superposition of the Fe(II)Fe(II) and Fe(III)Fe(III) spectra. The difference is clearly manifest by comparing the second derivatives of the



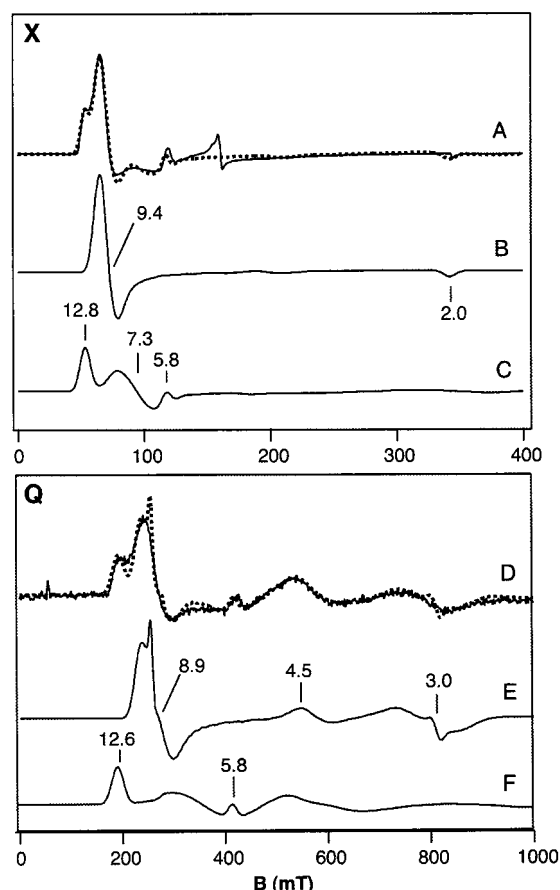


**Figure 8.** X-band (A–C) and Q-band (D–F) EPR spectra (solid lines) of **2b**. Simulations (dashed lines) comprise an equimolar mixture of two species (see Table 3 for the pertinent *zfs* parameters). See the legend of Figure 7 for experimental conditions.

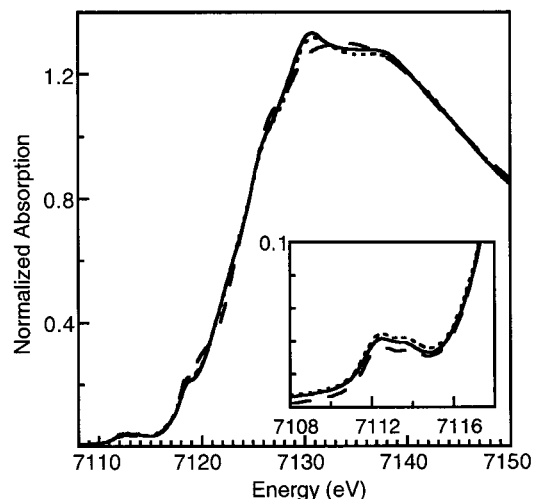


**Figure 9.** Fe K-edge and preedge transitions (inset) for  $[\text{Fe}_2(\mu\text{-O}_2\text{CAr}^{\text{Tot}})_4(4\text{-}^i\text{BuC}_5\text{H}_4\text{N})_2](\text{PF}_6)$  (**1b**) (—),  $[\text{Fe}_2(\mu\text{-O}_2\text{CAr}^{\text{Tot}})_4(\text{C}_5\text{H}_5\text{N})_2](\text{OTf})$  (**2b**) (⋯), and  $[\text{Fe}_2(\mu\text{-O}_2\text{CAr}^{\text{Tot}})_4(\text{THF})_2](\text{PF}_6)$  (**3b**) (---). Note the strong similarities in all three edges and preedges, suggesting similarities in their geometric and electronic structures, respectively.

K-edge spectra (Figure S3, Supporting Information), or more specifically, the second derivatives of the preedge region (Figure 11), which highlight individual transitions obscured by the rising edge absorption. Each of the compounds

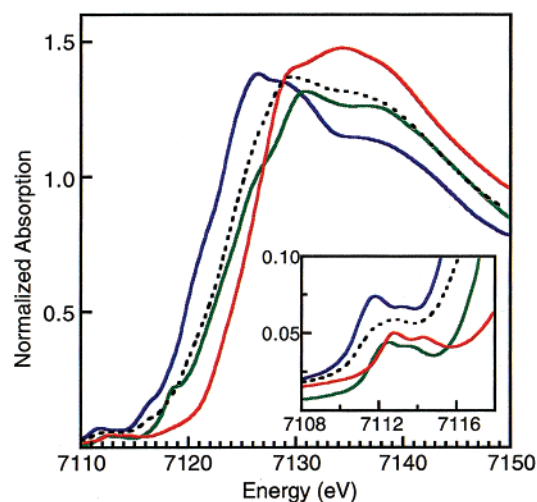


**Figure 10.** Fe K-edge and preedge transitions (inset) for  $[\text{Fe}_2(\mu\text{-O}_2\text{CAr}^{\text{Tot}})_4(4\text{-}^i\text{BuC}_5\text{H}_4\text{N})_2]$  (**1a**) (blue),  $[\text{Fe}_2(\mu\text{-O}_2\text{CAr}^{\text{Tot}})_4(4\text{-}^i\text{BuC}_5\text{H}_4\text{N})_2](\text{PF}_6)$  (**1b**) (green),  $[\text{Fe}_2(\mu\text{-OH})_2(\mu\text{-O}_2\text{CAr}^{\text{Tot}})_2(\text{O}_2\text{CAr}^{\text{Tot}})_2(4\text{-}^i\text{BuC}_5\text{H}_4\text{N})_2]$  (**1c**) (red), and a 50:50 weighted addition of the edges for the mixed-valence complex **1b** is intermediate in energy between edges for the related Fe(II)Fe(II) complex **1a** and Fe(III)Fe(III) complex **1c**, and comparable to the 50:50 weighted addition of these two edges. Also note that the mixed-valence complex has only two (rather than four) preedge features, which are likewise intermediate in energy between those for Fe(II)Fe(II) and Fe(III)Fe(III) species.

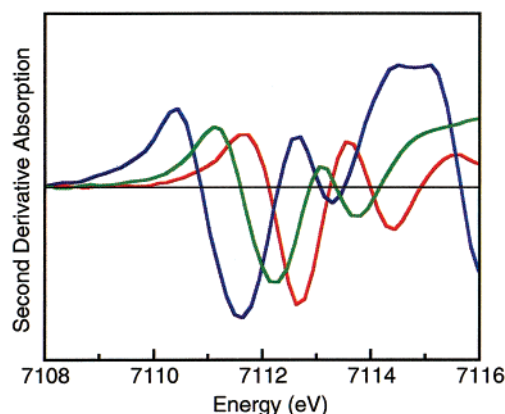


**Figure 11.** Second derivatives of the preedge region ( $1s \rightarrow 3d$  transitions) for  $[\text{Fe}_2(\mu\text{-O}_2\text{CAr}^{\text{Tot}})_4(4\text{-}^i\text{BuC}_5\text{H}_4\text{N})_2]$  (**1a**) (blue),  $[\text{Fe}_2(\mu\text{-O}_2\text{CAr}^{\text{Tot}})_4(4\text{-}^i\text{BuC}_5\text{H}_4\text{N})_2](\text{PF}_6)$  (**1b**) (green), and  $[\text{Fe}_2(\mu\text{-OH})_2(\mu\text{-O}_2\text{CAr}^{\text{Tot}})_2(\text{O}_2\text{CAr}^{\text{Tot}})_2(4\text{-}^i\text{BuC}_5\text{H}_4\text{N})_2]$  (**1c**) (red). Note that the spectrum for the mixed-valence species does not contain individual transitions at the same approximate energies of the related diiron(II) and diiron(III) complexes, as would be expected of a valence-localized complex. Rather, the two transitions for **1b** lie intermediate in energy to those for **1a** and **1c**.

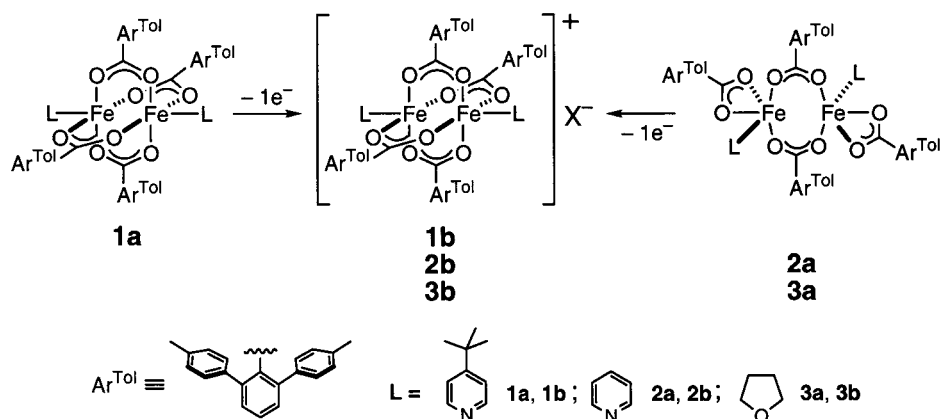
**1b–3b** has a pair of transitions in the preedge region, at energies that are almost exactly intermediate between those for **1a** and **1c**. This result suggests that the iron sites in each mixed-valence species are best described as delocalized Fe(2.5)Fe(2.5), rather than localized Fe(II)Fe(III). The spectrum for a localized complex should be the superposition of both Fe(II) and Fe(III) spectra.<sup>27c</sup>

## Discussion

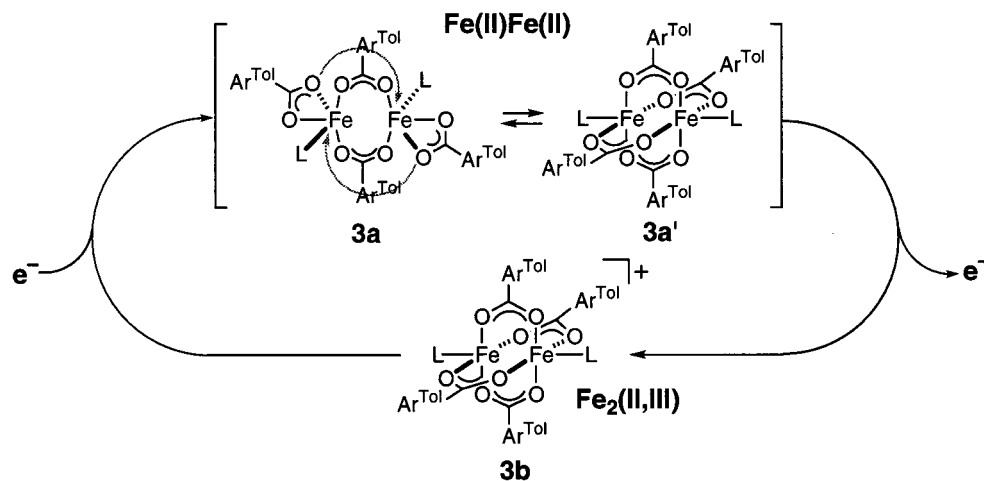
**Synthesis, Structures, and Spectroscopic Properties of Fe<sub>2</sub>(II,III) Complexes.** Synthetic routes to **1b–3b** are described in Scheme 1. Consistent with the oxidation poten-



Scheme 1



Scheme 2



tials determined for **1a** and **3a**, mixed-valence  $\text{Fe}_2(\text{II},\text{III})$  complexes **1b–3b** were readily accessed through one-electron oxidation by  $[\text{Cp}_2\text{Fe}]^+$  ( $E^\circ = +460$  mV vs SCE in  $\text{CH}_2\text{Cl}_2$ ) or  $\text{Ag}^+$  ( $E^\circ = +1110$  mV vs SCE in  $\text{CH}_2\text{Cl}_2$ ).<sup>45</sup> The redox behavior of **1a** and **3a**, as well as the structural outcome of their chemical oxidation, however, differs significantly.

Compound **1a** undergoes minimal structural rearrangement following oxidation to **1b**. Except for a slight but significant shortening of the  $\text{Fe}\cdots\text{Fe}$  distance from 2.8229(9)<sup>33</sup> to 2.713(3) Å, the coordination geometry afforded by the four  $\mu$ -1,3 bridging carboxylate and two N-donor ligands remains essentially identical. This behavior is consistent with the reversible interconversion between the  $\text{Fe}(\text{II})\text{Fe}(\text{II})$  and  $\text{Fe}(\text{II})\text{Fe}(\text{III})$  species observed by cyclic voltammetry of **1a** in  $\text{CH}_2\text{Cl}_2$  (Figure 2). In contrast, significant core rearrangement accompanies oxidation of the metal centers in **2a** and **3a**. Double carboxylate shifts<sup>46</sup> from terminal bidentate to  $\mu$ -1,3 bridging positions (Scheme 2) result in the significant shortening ( $\Delta_{\text{Fe}\cdots\text{Fe}} = 1.52\text{--}1.62$  Å) of the  $\text{Fe}\cdots\text{Fe}$  distances from 4.2189(13)<sup>34</sup> to 2.6982(13) Å (**2a**  $\rightarrow$  **2b**) and 4.2822(7)<sup>34</sup> to 2.6633(11) Å (**3a**  $\rightarrow$  **3b**). The irreversible electrochemical behavior of **3a** in  $\text{CH}_2\text{Cl}_2$  (Figure 3) most likely results from such a core rearrangement concomitant with a change in oxidation state.

The broad oxidation wave of **3a** initiates at  $-150$  mV, shifted by  $+180$  mV relative to that of **1a**. This shift is consistent with the coordination of less electron-donating (THF < 4-*tert*-butylpyridine) ligands to the metal. Compared with the broad oxidation wave, however, the corresponding reduction peak of **3a** is significantly narrower (Figure 3). This electrochemical behavior is nicely explained by the mechanism postulated in Scheme 2. In  $\text{CH}_2\text{Cl}_2$  at room temperature, **3a** exists as an equilibrium mixture with its quadruply bridged isomer **3a'**. Such a dynamic core rearrangement was demonstrated by VT  $^{19}\text{F}$  NMR studies of the related compound  $[\text{Fe}_2(\mu\text{-O}_2\text{CAr}^{4\text{-FPh}})_2(\text{O}_2\text{CAr}^{4\text{-FPh}})_2(\text{THF})_2]$ .<sup>40</sup> Electrochemical oxidation of multiple species at the electrode surface would account for the broad oxidation peak observed in the cyclic voltammogram. At the return potential, the diffusion layer mainly comprises a single species, **3b**, the one-electron reduction of which results in a well-defined and narrow cathodic peak. This behavior can be further evaluated by comparing the energies of the different structural isomers of  $[\text{Fe}_2(\text{O}_2\text{CAr}^{\text{Tol}})_4\text{L}_2]$  in different oxidation states. Such an investigation is in progress.<sup>47</sup>

The X-band EPR spectra of **1b–3b** are consistent with transitions originating within an  $S = 9/2$  manifold of an axial system. In these compounds, a plane is established at each

(45) Connelly, N. G.; Geiger, W. E. *Chem. Rev.* **1996**, *96*, 877–910.

(46) Rardin, R. L.; Tolman, W. B.; Lippard, S. J. *New J. Chem.* **1991**, *15*, 417–430.

metal center by the four oxygen atoms from the bridging carboxylate ligands. The  $z$ -axis of the  $D$  tensor is thus placed along the Fe–Fe vector. The  $D$  value in the  $S = 9/2$  Fe(II)–Fe(III) system has contributions from the Fe(II) and Fe(III) sites, as well as from the intramolecular Fe–Fe magnetic dipole interaction. For a  $S_{\text{tot}} = 9/2$  spin system arising from the coupling of a  $S = 5/2$  and a  $S = 2$  site, the system  $D$  value ( $D_{9/2}$ ) is described by eq 2. The intrinsic  $D$  value for

$$D_{9/2} = 0.167D_{\text{Fe(II)}} + 0.278D_{\text{Fe(III)}} + 0.278D_{\text{Fe–Fe}} \quad (2)$$

an Fe(III) site is usually  $\leq 0.5 \text{ cm}^{-1}$ . We also have determined that the contribution from the dipolar interaction is  $\leq 0.5 \text{ cm}^{-1}$ . Accordingly, if we ignore the small contribution from the last two terms, the  $D$  value for the Fe(II) site in **1b–3b** is approximately  $7 \text{ cm}^{-1}$ . Similar EPR signals have been previously observed for **A** (Figure 1), which displays an axial X-band signal with  $g_{\perp} = 10.2$  and  $g_{\parallel} = 2.3$ , fit using the zfs parameters  $D = 1.8 \text{ cm}^{-1}$  and  $E/D = 0.01$ .<sup>27b</sup> The X-band EPR spectra of the valence-trapped  $S = 9/2$  Fe(II)Fe(III) core in the cryoreduced RNR-R2<sup>26</sup> are described by the zfs parameters  $D = 1.5 \text{ cm}^{-1}$  and  $E/D = 0.05$ .<sup>44</sup>

**XAS: Valence-Delocalized Photoexcited States.** Central to our analysis of the XAS data in this investigation is the ability to prepare three diiron complexes having different oxidation states but similar N/O ligand combinations and coordination geometry. The effective electron density at the metal can be influenced by changes in the oxidation states or ligand composition, which lead to a shift in the X-ray absorption edge, and/or change in the edge shape, respectively.<sup>30</sup> By minimizing contributions from structural changes, the edge shift can be primarily correlated to the redox changes at the metal center.

The observed preedge XAS spectrum of **1b** is fully consistent with a valence-delocalized Fe(2.5)Fe(2.5) description, since the simple linear combination of Fe(II) and Fe(III) sites cannot reproduce the observed spectral pattern. The electronic coupling responsible for the valence delocalization in the ground state may be equally well operative in the X-ray photoexcited state. Previous L-edge XAS studies similarly revealed differences between valence-localized and -delocalized dinuclear Fe(II)Fe(III) complexes.<sup>27c</sup> The multiplet structures of spectra for the valence-trapped complexes were well modeled by 50:50 superpositions of L-edge spectra for related Fe(II)Fe(II) and Fe(III)Fe(III) complexes. The spectrum for the valence-delocalized compound **A**, in contrast, displays a broader and less well resolved multiplet structure. The corresponding Fe(II)Fe(II) or Fe(III)Fe(III) complexes, however, are not available for **A**, and a direct spectral comparison could not be made. To the best of our knowledge, compounds **1b–3b** represent the first examples of mixed-valence Fe<sub>2</sub>(II,III) complexes, where the valence-delocalized nature is apparently retained in excited states produced by X-ray absorption. With such proper calibrations made possible by the existence of structurally related Fe(II)–

Fe(II) and Fe(III)Fe(III) complexes, XAS should be able to probe the electronic structure of other mixed-valence Fe(II)–Fe(III) complexes.

**Valence Delocalization.** The parallel spin alignment of the Fe<sub>2</sub>(II,III) cores in **1b–3b** was confirmed by EPR studies and previous magnetic susceptibility measurements.<sup>31</sup> Electron delocalization in this  $S = 9/2$  spin system was indicated by the essentially identical geometric parameters obtained for the two iron atoms in the dimers in the solid state (Table 1). Although static disorder of valence-trapped Fe(II)Fe(III) cations or dynamic disordering due to rapid electron transfer between the metal centers<sup>48</sup> can equally well explain such structural results, Mössbauer<sup>31</sup> and XAS studies provide compelling evidence that the diiron(II,III) cores in **1b–1c** remain valence-delocalized at  $< 10 \text{ K}$ .

Such valence delocalization between paramagnetic centers is described by double exchange,<sup>14,15,23,49</sup> a mechanism by which delocalized electrons provide an additional coupling mechanism for the parallel alignment of the spins. Such resonance interaction between metal centers can be mediated either by direct metal–metal orbital overlap or by the bridging ligands. Notable structural features of the previously characterized valence-delocalized Fe<sub>2</sub>(II,III) compounds **A–C** (Figure 1) include short metal···metal distances and the presence of single-atom bridging ligands. Oxygen atoms supplied by hydroxo, phenoxo, or alkoxo ligands promote the short Fe···Fe distances of 2.509(6)–2.7414(8) Å in **A–C** and can mediate a strong metal–metal resonance interaction. Theoretical studies indicate that a direct  $\sigma$ -type overlap of the two  $d_{z^2}$  orbitals is responsible for the valence delocalization in **A**,<sup>27d</sup> whereas both  $\sigma$ -type interaction between the Fe  $d_{x^2-y^2}$  orbitals and Fe–O<sub>phenoxide</sub> bonding contribute to the similar phenomenon in **B**.<sup>28b</sup>

Although compounds **1b–3b** feature short Fe···Fe distances comparable to those in **A–C** (Table 2), their quadruply bridged Fe<sub>2</sub>(II,III) cores lack efficient coupling pathways afforded by single-atom bridging ligands. Double exchange observed in the [Fe<sub>2</sub>( $\mu$ -O<sub>2</sub>CAr<sup>Tol</sup>)<sub>4</sub>L<sub>2</sub>]<sup>+</sup> module is thus apparently mediated by the direct through-space interaction between the metal centers. Preliminary DFT calculations indicate that  $\pi$ -type overlap between  $d_{xz}$  orbitals is responsible for the strong electron delocalization in **1b–3b**, the details of which are currently under investigation.<sup>50</sup> Collectively, the synthesis and characterization of **1b–3b** significantly expands the class of valence-delocalized diiron(II,III) clusters, affording a novel basis for correlating the geometric and electronic factors responsible for this novel phenomenon.

**Acknowledgment.** This work was supported by grants from the National Science Foundation and the National Institutes of Health. Stanford Synchrotron Radiation Laboratory operations is funded by the Department of Energy, Office of Basic Energy Sciences. The SSRL Structural

(48) Achim, C.; Bominaar, E. L.; Staples, R. J.; Münck, E.; Holm, R. H. *Inorg. Chem.* **2001**, *40*, 4389–4403.

(49) Noodleman, L.; Baerends, E. J. *J. Am. Chem. Soc.* **1984**, *106*, 2316–2327.

(50) Rodriguez, J. H.; Lee, D.; Lippard, S. J. Unpublished results.

(47) Baik, M.-H.; Lee, D.; Lippard, S. J.; Friesner, R. Unpublished results.

Molecular Biology Program is supported by the Department of Energy, Office of Biological and Environmental Research, and by the National Institutes of Health, National Center for Research Resources, Biomedical Technology Program. We thank Mr. C. M. Chang of the Nocera group at MIT for assistance in acquiring the NIR spectra.

**Supporting Information Available:** Cyclic voltammograms of  $[\text{Fe}_2(\mu\text{-O}_2\text{CAr}^{4\text{-FPh}})_4(4\text{-}^t\text{BuC}_5\text{H}_4\text{N})_2]$ , NIR spectra of **1b**, and second derivatives of the K-edge spectra for **1a**, **1b**, and **1c**. This material is available free of charge via the Internet at <http://pubs.acs.org>.

IC011050N